Toward Controlled Flight of the Ionocraft: A Flying Microrobot Using Electrohydrodynamic Thrust With Onboard Sensing and No Moving Parts

Daniel S. Drew , Nathan O. Lambert , Craig B. Schindler , and Kristofer S. J. Pister

Abstract—**This letter presents an insect-scale microrobot that flies silently and with no mechanical moving parts, using a mechanism with no analogue in the natural world: electrohydrodynamic thrust produced by ions generated via corona discharge. For the first time, attitude and acceleration data are continuously collected from takeoff and sustained flight of a 2 cm × 2 cm, 30 mg "ionocraft" carrying a 37 mg 9-axis commercial IMU on FlexPCB payload, with external tethers for power and data transfer. The ionocraft's steady-state thrust versus voltage profile, dynamic response to a time-varying signal around a high voltage dc bias point, and aerodynamic drag at incident angles around 90° are measured. These experimental measurements, as well as measured IMU sensor noise, are inserted into a MATLAB Simulink simulation environment. Simulation shows controlled hovering and planned flight in arbitrary straight trajectories in the *XY* plane.**

Index Terms—**Micro/nano robots, aerial systems: mechanics and control, mechanism design, electrohydrodynamic force, corona discharge.**

I. INTRODUCTION

INSECT-SCALE flying microrobots are an emerging class of autonomous systems with potential use cases in disaster exploration and recovery, precision agriculture, surveillance, and swarm interfaces [1]–[3]. Development of these pico air vehicles has accelerated in recent years, with biomimetic designs demonstrating enough thrust for self-lifting using both piezoelectric and electromagnetic actuators [4]–[6]. While flapping wing mechanisms are proven to function in nature down to the centimeter scale, they require both complicated mechanical transmissions and novel controller designs. Conversely, the flying microrobot described in this letter uses a mechanism with no natural analogue, electrohydrodynamic (EHD) force, in order to fly. The ability to produce thrust with no mechanical moving parts simplifies fabrication and design, while the nature of the produced thrust allows for controller design similar to a standard quadcopter.

Electrohydrodynamic force is produced by the collisions of moving charged particles with a neutral fluid (Fig. 2). Derivations for an ideal EHD actuator project a maximum thrust on the order of 100 N/m^2 at a thrust efficiency of 2 N/kW [7]. Around the time of its first published full-fledged theoretical description in 1967, EHD thrust was proposed as a way to produce flying human-scale craft [8]. Unfortunately, the aerial force densities are too low to realistically support the endeavour of flight with human passengers. However, because EHD thrust is fundamentally produced by electrostatic forces, it is scale invariant and leads to at least two theoretical benefits for decreasing the scale of thrusters: the thrust to weight ratio will increase and the operating voltage to achieve a desired drift field strength will decrease. Corona discharge, the most common source of ions for atmospheric EHD thrust, is a well-studied atmospheric plasma mechanism caused by avalanche breakdown ionization of neutral fluid in a high strength electric field. Using highly asymmetrical electrodes allows for localized plasma generation around the one with a higher local electric field (e.g. a sharp tip) and a subsequent ion current without full dielectric breakdown.

Microfabricated electrohydodynamic thrusters based on a corona discharge effect have previously been characterized to assess compliance with scaling laws [9], and have been shown to produce sufficient force for takeoff when incorporated into an airframe [10]. In this work, we present an electrohydrodynamic thrust powered centimeter-scale flying robot (Fig. 1) that is capable of flight while carrying and streaming data from a commercial 9-axis IMU. Experimental values for aerodynamic drag, actuator dynamics and response, and sensor noise are measured and inserted into a simulation environment to demonstrate the possibility for and limits of controlled flight of this system.

II. RELATED WORK

Current state of the art flying microrobots are largely classified as "Flapping Micro Air Vehicles", or FMAV. Self-lifting FMAV have been developed using piezoelectric [5], electromagnetic [6], and electrostatic [11] actuators to drive mechanical transmissions and subsequent flapping motion of the wings. In contrast, the use of EHD force as a thrust mechanism obviates the need for a separate transmission or dedicated lift surface (e.g. a wing), increasing potential thrust to weight ratio.

Work on the ionocraft is currently following a trajectory (static thrust measurement, open-loop takeoff, controlled
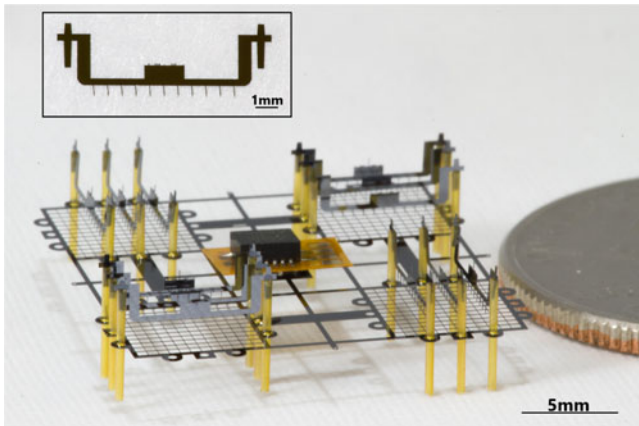
Fig. 1. An assembled ionocraft next to a United States quarter. The ionocraft itself is approximately 2 cm by 2 cm and masses 30 mg. Also shown is the 37 mg FlexPCB board with 9-axis IMU and associated passives attached to the center of the airframe. The ionocraft is built from 41 discrete components, each connected by a combination of mechanical slots and UV-curable epoxy. Inset: A single emitter electrode. The 500 μm long, 5deg tip angle lithographically defined asperities are aligned with the grid and used to reduce operating voltage.

Fig. 3. 3D model renders of the assembly process. (1) Pre-cut silica tubes are inserted into slots in a CNC-milled aluminum jig. (2) The ionocraft airframe is slid down the guiding posts. (3) The emitter wires are rotated out of plane and tapered guides are inserted into the silica tubes. The distance between the emitter wires and collector grid is now determined by a combination of lithography, the length of the silica tubes, and the depth of the guide slots milled into the jig. (4) Silicon "jumpers" are lowered onto guide posts on the emitter wires. These both help with alignment between adjacent emitter wires and serve as electrical connection points after application of silver epoxy.
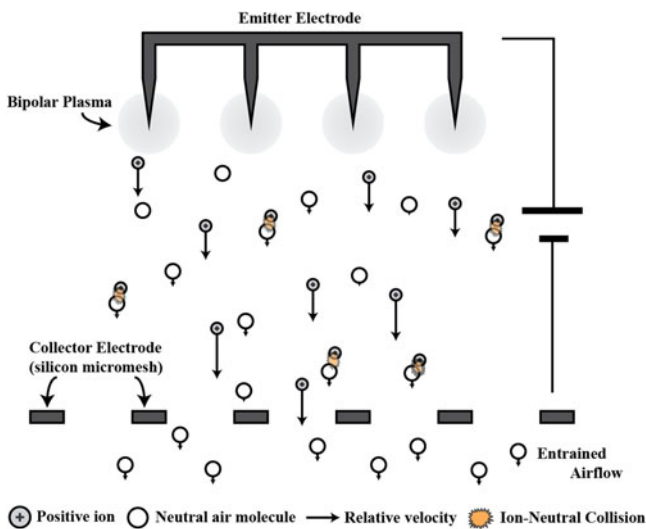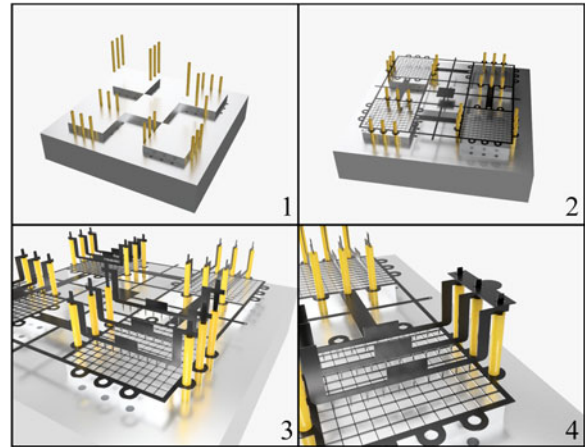

Fig. 2. Schematic depiction of the cross-sectional view of an emitter wire and collector grid electrode pair. Thrust is produced when ions, drifting in the applied electric field, collide with neutral air molecules and impart momentum. Bipolar ions are generated in the corona plasma region localized at the sharp tips of the emitter electrode, but only positive ions (mainly N_2^+) will drift towards the collector grid.

hovering, controlled flight) previously demonstrated by the Harvard RoboBee [5], [12], [13]. Similarly, continuous design improvements have been made to enhance performance metrics such as thrust density and operating voltage, as well as incorporating more on-board capabilities.

Simulations designed to verify actions in novel robotics platforms have become a common practice in the field, with [14] showing the benefits of characterizing the system at a computational level where tests are "free." The simulation we present in this letter was inspired from the Simulink simulation from the work of Mahony *et al.* in [15].

Despite being well understood and controllable systems, standard quadcopters are underactuated, meaning the system has more degrees of freedom than control inputs. Our robot is further underactuated due to a lack of body frame rotational coupling from the motors (discussed in IV). Recently, control of a flying vehicle with a single moving part [16] as well as control of a quadcopter with broken propellers [17] has been demonstrated. Additionally, nonlinear control of underactuated mechanical systems has been studied extensively [18].

III. EXPERIMENTAL RESULTS

A. Device Fabrication and Assembly

The robots are made using active electrodes fabricated in standard MEMS wafer-scale silicon processes as well as commercially available silica tubing. A silicon-on-insulator wafer with 40 μm device thickness forms the substrate for a single-mask deep reactive ion etch and subsequent vapor-phase hydroflouric acid release etch. Thin tether structures are broken manually to yield fully released, 40 μm thick emitter and collector electrodes that can be removed from the wafer surface for assembly. Fused-silica capillary columns, typically used for gas chromatography, are the dielectric standoffs between the electrodes.

Assembly of the robots (Fig. 3) involves standard surface-mount technology (SMT) practices performed under a dissection microscope. Electrodes are moved and placed by a combination of a small diameter vacuum wand and tungsten micromanipulator probes. Mechanical connections and alignments are handled by a combination of geometric tolerances and UV-curable epoxy applied via a micromanipulator probe. Electrical connections are formed by silver epoxy applied via a pneumatic fluid dispensing system and cured on a hot plate. A CNC-milled aluminum fixture is used to keep the device in place and provide alignment aid for various components.
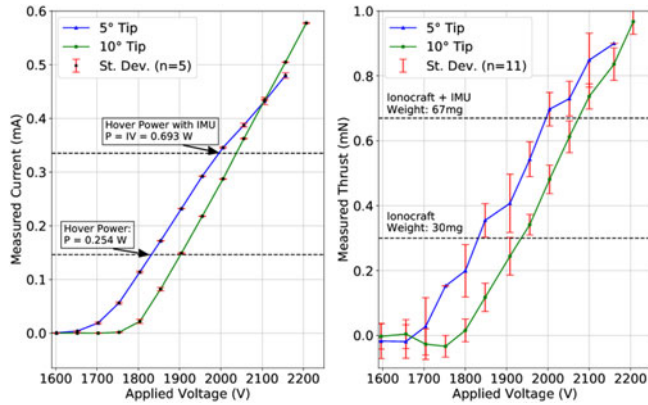
Fig. 4. Plots showing measured current (left) and measured output force (right) of the ionocraft as a function of its input voltage. The upper horizontal line shows the current (left) and force (right) required for hovering with the IMU onboard. The lower line shows the current and force needed for takeoff without the IMU. While collecting this data, all four of the thrusters were electrically connected. Tip angle refers to the nominal apex angle of the lithographic asperities on the emitter wires.

A Flex PCB board was designed to contain a commercial 9-axis IMU, the InvenSense MPU-9250, as well as three associated passives and bonding pads. The board's 6 mm by 6.5 mm footprint allows it to be fixed in place via UV-curable epoxy in a designated central region of the robot airframe without interfering with the surrounding thrusters.

B. Actuator Response

To measure output force, the ionocraft is mounted on an acrylic post fixed directly to a Phidgets 100 g Micro load cell. Multiple instruments are controlled via GPIB for synchronized force-current-voltage sweeps.

The canonical expression for electrohydrodynamic force based on an ideal 1D model together with a constant factor, β, is given in (1), where d is the ion drift distance and μ is the ion mobility in air (approximately 2e-4 m^2/Vs for N_2^+ in dry air). The β factor accounts for losses in the system that arise as a combination of indirect ion field paths (loss of vertical output force to horizontal momentum transfer), ratio of plasma sheath size to drift gap, and aerodynamic drag on the collector grid,

$$F = \beta \frac{Id}{\mu} \qquad (1)$$

Sets of emitter wires with both 5 and 10 degree nominal tip angles (tips visible in Fig. 1 inset) were fabricated. Decreasing the lithographically defined tip angle from 10 to 5 degrees was shown to decrease corona discharge onset voltage by about 100V without a significant affect on the IV relationship following plasma ignition (Fig. 4). Prior work has measured a loss factor of about 50% ($\beta = 0.5$) using similar microfabricated silicon electrodes [9]. Direct measurement of output force as a function of applied voltage and ion current (Fig. 4) in this work yield a β of approximately 0.8 for the 5 degree emitter tips and 0.7 for the 10 degree emitter tips.

A 1 mN total output force from four 6 mm × 6 mm collector grids corresponds to a thrust density of about $7N/m^2$, a similar
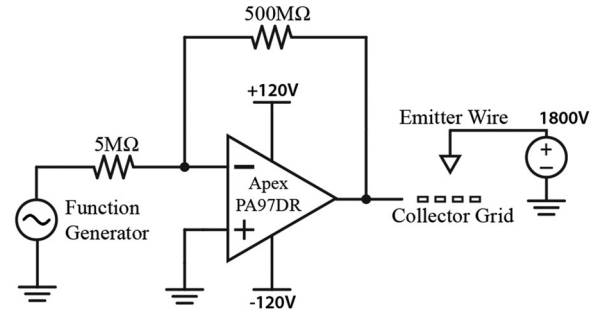

Fig. 5. Circuit schematic of the actuator dynamic response test setup. A high voltage op-amp is used to modulate the control inputs around a DC bias point by raising and lowering the voltage of the collector grid.
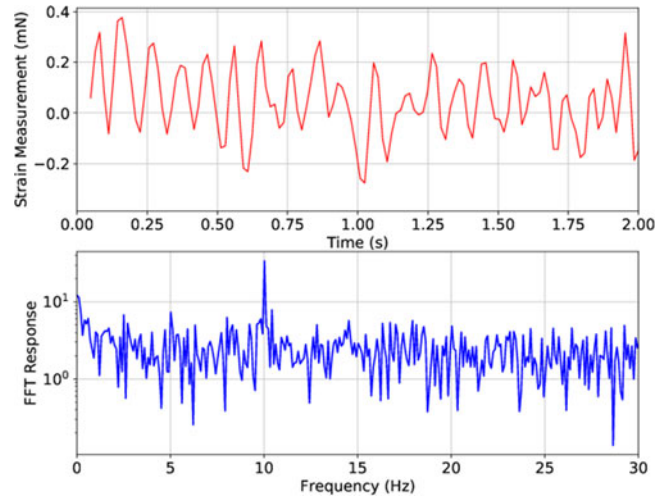

Fig. 6. The output force from an ionocraft with a 1800V DC bias applied to the emitter wires and a 200 V peak-to-peak, 10 Hz sine wave applied to the collector grids. The data is collected with a sampling period of 16 ms. Top: Measured output force with DC bias force (approximately 0.22 mN) and weight of the ionocraft subtracted, then filtered by a digital 20 Hz cutoff low pass filter. Bottom: A Fourier transform of the zero centered, unfiltered strain data shows the distinct 10 Hz peak.

value to prior work despite an increased emitter wire density. It is possible that the emitter wire spacing of approximately 1.5 mm is too high and should be brought to a value between 40% and 80% of the electrode gap distance (500 μm) for an optimal thrust density increase, as shown in work on larger electrode gap EHD systems [19].

A high voltage amplifier circuit (Fig. 5) was created for testing the dynamic response of the ion thrusters. First, a positive DC voltage above the corona discharge initiation is applied to the emitter electrode with the collector electrode held at ground. Next, a $2V_{pp}$ sine wave produced by a function generator at the input of the amplifier is transformed by the amplifier gain of 100 into a high voltage (200 V_{pp}) signal.

The ionocraft was shown to successfully track sine wave inputs with frequency up to 10 Hz (Fig. 6). Significant measurement noise, with magnitude higher than the forces attempted to be resolved, precluded experimentation without the load cell's custom-built data capture accessory (PhidgetBridge). The sampling frequency limitations of this accessory made experiments
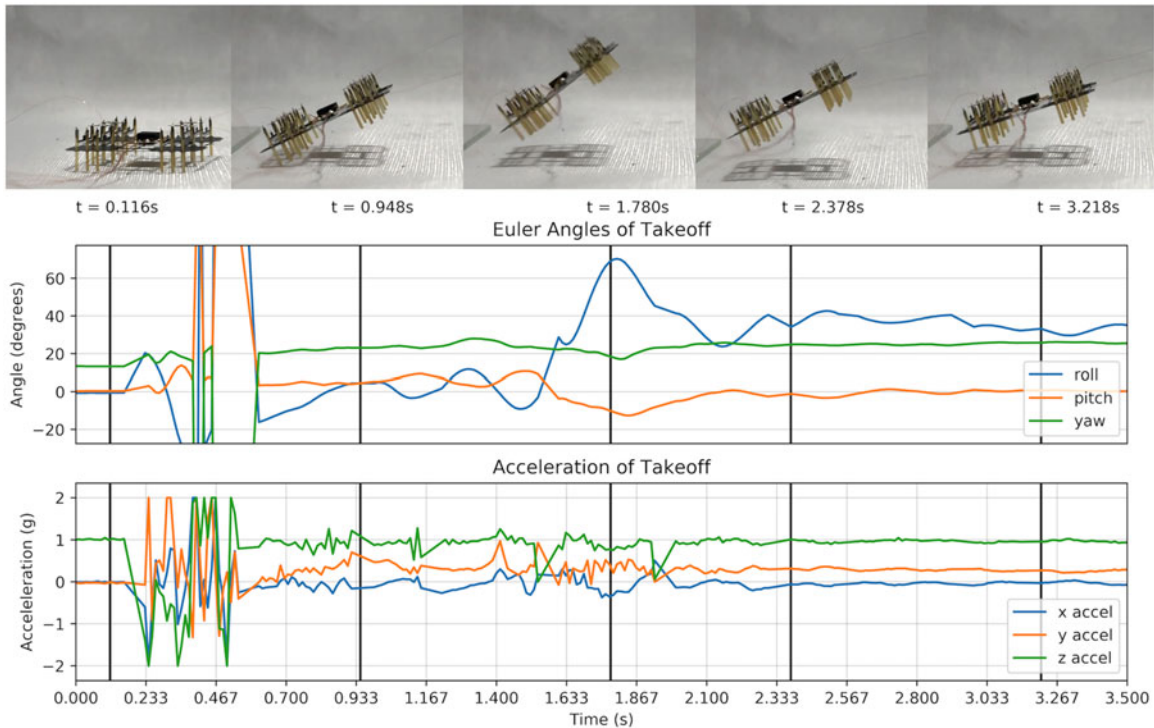
Fig. 7.   Open-loop, uncontrolled takeoff of the ionocraft while carrying an InvenSense MPU-9250, a state of the art 9-axis IMU. The IMU is reporting accelerations and Euler angles at roughly 100 Hz, the latter of which is calculated using InvenSense's proprietary MotionFusion algorithm on-board the IMU. Each image of the ionocraft was taken at the time corresponding to the black line below it. Erratic transient response from the IMU at the time of high voltage application indicates that further electromagnetic shielding may be necessary.

at frequencies above 10 Hz impossible. Future work will develop a more stable testing platform for $>$100 Hz dynamic response characterization that can resolve forces on the order of 10 μN.

C. Tethered Flight With Onboard Sensor

Takeoff while streaming attitude and acceleration data from the on-board 9-axis IMU was demonstrated (Fig. 7). Liftoff occurred at approximately 2000 V — over 20% lower than prior work which did not contain an onboard sensor package [10]. There are a total of seven external wires: two high voltage lines to the emitter wires (the two other thrusters are connected internally); power, ground, and two data wires to the IMU FlexPCB; and a separate ground connection to the airframe. A common issue in the field of microrobotics is that the spring force of the external tethers required for power and control tends to overpower the system due to the robot's relatively low mass and output force, preventing movement. The external wires in this case confer a degree of stability during open-loop flight that prevents an immediate failure like twisting in its own tethers, but the robot is still both unstable (high body angle oscillations) and able to return to landing on the ground when power is no longer applied. Although future work will strive to decrease the number of external tethers and therefore their contribution to body dynamics, the first instances of controlled flight will certainly be under tethered power; this demonstration of takeoff despite the external tether forces is encouraging.

The open-loop flight is synchronized with the streaming sensor readings during post-processing. Takeoff and landing
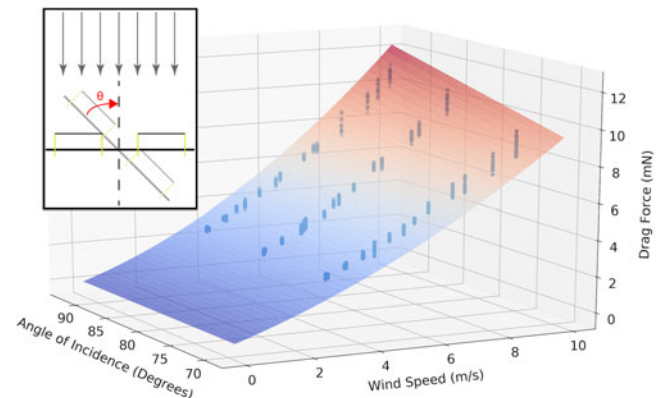

Fig. 8.   Plot of the wind tunnel drag data shown with a fitted hyperplane using (3). The upper left diagram shows the definition of angle of incidence.

cycles were repeated up to five times with a single robot without failure, although the IMU had to be restarted after a landing where the ionocraft had flipped completely over before touching down.

D. Aerodynamic Drag

A miniature low-speed wind tunnel, designed using ANSYS FEA software and constructed from a combination of laser cut and 3D printed parts, is used to characterize aerodynamic drag on the ionocraft. The full tunnel is about 1.5 meters long, with a 10 cm $\times$ 10 cm $\times$ 20 cm test chamber. A manually controlled variable-speed fan is calibrated using a TSI AVM430 hot wire
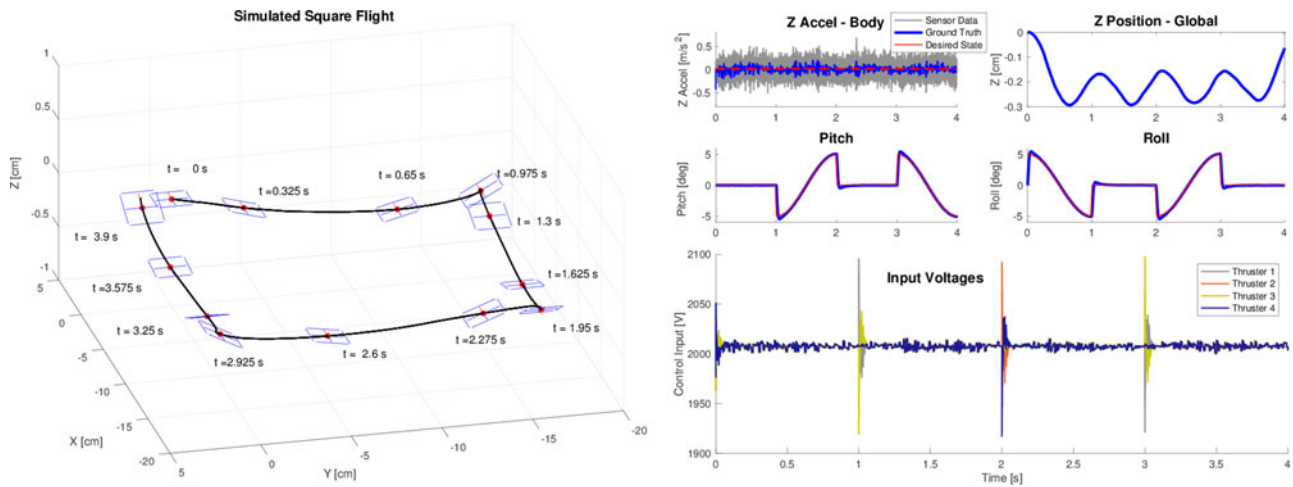
Fig. 9. Left: A simulated flight of the ionocraft over a 4 second flight about a square. The square is navigated by supplying sinusoidal profiles as desired states to pitch and roll controllers independently, and the trajectory of its center of mass is shown in the dotted black line. Right: Control inputs and state variables for the simulated flight. Note that global Z position is only for evaulating simulation performance, and is not a variable being controlled. The pitch and roll measurements have noise, but the magnitudes are substantially lower than the controlled movement.

anemometer inserted through an inlet in the test chamber. The ionocraft is mounted on an adjustable acrylic sting using epoxy applied to the center pad of the airframe. The sting attaches directly to a Phidgets 100 g Micro load cell.

Experimental measurements of drag force F_D versus wind speed v and angle of incidence θ are fit to a hyperplane, as shown in Fig. 8. The region of measurements collected are $v \in [0, 10)$ (m/s) and $\phi = 1 - \theta \in [0, \frac{\pi}{6})$ radians. We model the drag at this wind speed as being of the form

$$F_D(v) = av^2 + bv \ [mN] \tag{2}$$

where the constants a and b are parameters of ϕ, resulting in the drag function $F_D(v, \phi)$. Fitting the a and b to a first order polynomial to match the common approximations $\sin(\phi) = \phi$, $\cos(\phi) = 1 - \phi$ for $0 \leq \phi \ll 1$, we get a parametric function of the form:

$$F_D(v, \phi) = (a_1\phi + a_2)v^2 + (b_1\phi + b_2)v \ [mN] \tag{3}$$

Fitting with ordinary least squares returns the following parameters:

$$a_1 = -.0558 \quad b_1 = -.0201$$
$$a_2 = .1305 \quad b_2 = .6275$$

The drag fit yields a maximum vertical (90 degree angle of incidence) airspeed of 1.26 m/s; this corresponds to a drag force of 1mN, which is equal to the maximum thrust the ionocraft is capable of producing. The measured values used to create the hyperplane are above 3 m/s due to the difficulty of reliably generating low speed laminar flow in the wind tunnel.

IV. MODEL AND CONTROLLED FLIGHT SIMULATION

A. Dynamics Model

The dynamics of a quadcopter are well studied and understood [15], [20]. We begin this section by first discussing the quadcopter model. A quadcopter's four individually controllable

thrusters each generate a force F_i resulting in a body fixed-frame z-axis thrust, T, and body fixed-frame torques τ_x, τ_y, and τ_z, as shown in (4). The constant c is a coupling factor between the motor forces and the τ_z. The parameters l_x and l_y are defined as the distance from the thruster's center to the body fixed-frame's center of mass in the x and y directions, respectively. We use a north-west-up axis orientation.

Because a quadcopter's four thrusters are propeller based, and therefore generate angular momentum, the coupling factor c is non-zero. It can then be seen that the matrix in (4) is full rank, and therefore control of T_z, τ_z, τ_y, and τ_x are decoupled.

$$\begin{bmatrix} T_z \\ \tau_z \\ \tau_y \\ \tau_x \end{bmatrix} = \begin{bmatrix} 1 & 1 & 1 & 1 \\ -c & c & -c & c \\ -l_x & -l_x & l_x & l_x \\ -l_y & l_y & l_y & -l_y \end{bmatrix} \begin{bmatrix} F_1 \\ F_2 \\ F_3 \\ F_4 \end{bmatrix} \tag{4}$$

The ionocraft model is the same as the quadcopter model, with one important exception — the ionocraft uses ion thrusters instead of propeller based thrusters (i.e., the ionocraft thrusters do not generate angular momentum) and the therefore the coupling constant c is equal to 0. Accordingly, the matrix in (4) is *not* full rank and control authority of τ_z (i.e. yaw control) is lost.

The ionocraft thrust forces, assumed to be point forces at the corners of the robot, along with drag, are the only forces applied in the model; the tether wires are not incorporated in the dynamics. The assumption of thrust being a point force holds when the force distribution over the collector grid is uniform; in reality, the EHD force is not axisymmetric but instead expected to decrease with distance from the emitter wires (i.e., in the x direction if the wires are assumed to lie along the y axis) as some function of the device electrostatic solution.

B. Controller Design

Hovering and basic open loop trajectories only require data streamed from the 9-axis IMU. To hover, the controller regulates
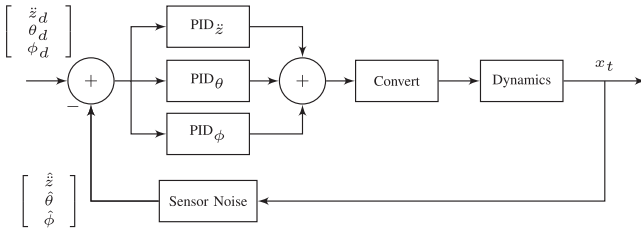
Fig. 10.   Overall structure of the control scheme. The errors between the estimates of vertical acceleration, pitch, and roll ($\hat{\ddot{z}}$, $\hat{\theta}$, and $\hat{\phi}$, respectively) and the desired states $\ddot{z}_d$, θ_d, and ϕ_d are fed through three PID controllers. The outputs of the controllers are then converted into a vector input as shown in (5). Not shown is a saturation block that prevents the thrusters from trying to apply more force than the maximum value before breakdown (approximately 0.25 mN per thruster).

$\ddot{z}$, pitch, and roll to zero. The equilibrium input for each individual thruster is $F_{eq} = \frac{mg}{4}$. The outputs $u_{\ddot{z}}$, u_θ, and u_ϕ of the PID controllers (shown in Fig. 10) are used to drive the system to desired vertical acceleration, desired pitch, and desired roll, respectively, where $\vec{F}$ is the vectorized input containing all four thruster forces.

$$\vec{F} = \begin{bmatrix} F_{eq} \\ F_{eq} \\ F_{eq} \\ F_{eq} \end{bmatrix} + \begin{bmatrix} 1 \\ 1 \\ 1 \\ 1 \end{bmatrix} u_{\ddot{z}} + \begin{bmatrix} -1 \\ -1 \\ 1 \\ 1 \end{bmatrix} u_\theta + \begin{bmatrix} 1 \\ -1 \\ -1 \\ 1 \end{bmatrix} u_\phi \quad (5)$$

Each thruster has a maximum force it can provide (approximately 0.25 mN); this saturation makes each thruster nominally non-linear. The PID controllers are tuned around equilibrium so that the controlled forces stay well away from saturation within tested operation.

Yaw actuation can be achieved by quick, repeated sequences of "pitch and then roll." Simulation demonstrates this approach achieving a yaw rate of up to ± 10 deg/s while still maintaining stable hover. This method comes at the cost of up to 10 cm/s X-Y drift because of the lack of simultaneous decoupled control of $\ddot{x}$ and $\ddot{y}$. Future formalization of this "pitch and roll" method with Lie brackets (as in [21]) could lead to a closed-loop non-holonomic yaw controller.

C. Flight Simulation

The experimental drag data and voltage to force mapping, as well as the sensor noise discussed below, are included in the simulation model. The simulation dynamics time-step is 10 μs. This is sufficient, because if the ionocraft rolls or pitches by applying the maximum thrust that it is capable of producing (approximately 0.5 mN by firing two of its thrusters simultaneously and leaving the other two off), it would change roll or pitch angles by fewer than 10^{-4} degrees within one simulation time-step. The measurement and hand-tuned PID control blocks update at 100 Hz, which is the sample rate used when collecting experimental flight data with the MPU-9250 9-axis IMU with the MotionFusion algorithm on [22]. The documented noise power from the IMU on $\ddot{x}, \ddot{y}, \ddot{z} = 300$ μg/$\sqrt{\text{Hz}}$. The noise power on the Euler angles is undocumented for the Digital Motion Processing unit. Direct measurement of the noise power of

a stationary signal is 25 nrad/$\sqrt{\text{Hz}}$. During the simulation, we increase the Euler angle noise power by a factor of 40x as well as increase the accelerometer noise power by a factor of 10x. These increases provide overestimates of the noise signals in order to better prepare for future controlled flight of a fabricated device outside a laboratory setting.

Open loop maneuvers have been encoded to demonstrate the future potential of controllability over arbitrary shapes in the X-Y plane. The simulation results, shown in Fig. 9, shows a square flight pattern, control input, noisy states, and true state variables. Because direct measurements of the global positions X, Y, and Z are unavailable, the global positions drift over time. The raw accelerometer data for $\ddot{z}$ provides a reference for maintaining altitude. However, the global Z position is only controlled by the local $\ddot{z}$ reading, so it does not exactly track gravity when pitch and roll are non-zero. This global Z drift is compensated for by controlling to a desired state of $\ddot{z} = .015$ m/s^2.

Disturbance characterization of the system is not included because the currently collected drag data does not account for resultant body torques. Without characterizing these moments, any planar disturbance will only cause drift and will not test roll or pitch stability; subsequent drift recovery is not possible with the current implementation due to the lack of global position data.

Separate simulations with variation in force produced by each thruster (e.g. from fabrication variation) at a given controller-outputted input voltage show loss of X-Y controllability above 1% variation and loss of hover functionality at 10% force variation. This is due to the hand-tuned PID controllers and could be improved with either more robust controllers or an in-line calibration method prior to takeoff.

V. Conclusion and Future Work

Although initial demonstrations of controlled flight will certainly be tethered and in an indoor laboratory setting, we envision the future ionocraft as a fully autonomous robot capable of outdoor flight. The path towards autonomy requires making strides in a number of interdependent categories, including: system development to allow for incorporation of more onboard computation, control, and sensing electronics; further engineering refinement of the EHD actuator to provide increased thrust density and efficiency at a lower operating voltage; and further development of both the simulation environment and the bench-scale flight testing setup to begin development of more robust controllers with high level functionality (e.g. trajectory planning).

Validation of using a high voltage time varying signal in tandem with an applied DC bias above the corona discharge initiation point to modulate thrust indicates that a future low mass power and control circuit could use a similar topology to Karpelson *et al.* [23], [24]. A low mass optical flow sensor similar to one fabricated in [25] could be used in conjunction with IMU data to stabilize absolute position as well as attitude. Assuming a single Flex PCB could be shared for the 9-axis IMU, control ASIC, driver circuit, and optical flow sensor, a total mass budget on the order of 100 mg could be expected. This should be

well within the capabilities of future ionocraft designs, opening the door for controlled flight of a 2 cm by 2 cm microrobot with only high voltage DC bias, low voltage (for ICs), and ground wires, with no external sensors. Autonomous flight will require incorporation of high energy density research-grade batteries; even then, actuator performance will need to be improved to make this feasible.

The aerial thrust density measured in this work is still far below the theoretical maximum. Further, while increasing the number of emitter wires per thruster improved the maximum force output compared to prior work, it did not come with a large benefit to thrust-to-weight ratio. Future designs should look to maximize thrust density by increasing the number of emitter tips per collector grid and optimizing the tip spacing; they should also include mechanical affordances to decrease the number of required adhesive joints and additional components per emitter wire. Process development to further enhance the electrode geometric asymmetry (e.g. by creating tips with lower radii of curvature) should both decrease the required voltage for flight as well as allow for operation in a higher efficiency regime at the cost of output force.

Future work on the simulation will be to implement trajectory optimization and path planning for arbitrary states as well as to incorporate stability guarantees on motion. A nonholonomic or nonlinear controller for yaw positioning will be a substantial step towards controlling trajectories. Alternatively, the addition of angled or perpendicular thrusters would give a full rank controllability Gramian and the option of other optimal control solutions. The simulation environment will serve as the groundwork for developing a model of disturbance rejection in autonomous flight, potentially leveraging insight from similar work on the RoboBee [12] [26] for strategies to provide disturbance stability at the centimeter scale. Further characterization of the drag and lift coefficients will be needed before detailed exploration of this area, potentially by mounting devices on a six-axis force-torque sensor inside the low speed wind tunnel instead of a single axis strain sensor.

REFERENCES

[1] A. M. Flynn, "Gnat robots (and how they will change robotics)," Massachusetts Institute of Technology Working Paper, vol. 295, Jun. 1987.

[2] M. Brambilla, E. Ferrante, M. Birattari, and M. Dorigo, "Swarm robotics: A review from the swarm engineering perspective," *Swarm Intell.*, vol. 7, no. 1, pp. 1–41, 2013.

[3] D. Floreano and R. J. Wood, "Science, technology and the future of small autonomous drones," *Nature*, vol. 521, no. 7553, pp. 460–466, 2015.

[4] R. J. Wood *et al.*, "Progress on picoair vehicles," *Int. J. Robot. Res.*, vol. 31, no. 11, pp. 1292–1302, 2012.

[5] R. J. Wood, "The first takeoff of a biologically inspired at-scale robotic insect," *IEEE Trans. Robot.*, vol. 24, no. 2, pp. 341–347, Apr. 2008.

[6] Y. Zou, W. Zhang, and Z. Zhang, "Liftoff of an electromagnetically driven insect-inspired flapping-wing robot," *IEEE Trans. Robot.*, vol. 32, no. 5, pp. 1285–1289, Oct. 2016.

[7] L. Pekker and M. Young, "Model of ideal electrohydrodynamic thruster," *J. Propulsion Power*, vol. 27, no. 4, pp. 786–792, 2011.

[8] E. A. Christenson and P. S. Moller, "Ion-neutral propulsion in atmospheric media." *AIAA J.*, vol. 5, no. 10, pp. 1768–1773, 1967.

[9] D. Drew, D. S. Contreras, and K. S. Pister, "First thrust from a microfabricated atmospheric ion engine," in *Proc. IEEE 30th Int. Conf. Electro Mech. Syst.*, 2017, pp. 346–349.

[10] D. S. Drew and K. S. Pister, "First takeoff of a flying microrobot with no moving parts," in *Proc. Int. Conf. Manipulation, Autom. Robot. Small Scales*, 2017, pp. 1–5.

[11] X. Yan, M. Qi, and L. Lin, "Self-lifting artificial insect wings via electrostatic flapping actuators," in *Proc. 28th IEEE Int. Conf. Micro Electro Mech. Syst.*, 2015, pp. 22–25.

[12] Z. E. Teoh, S. B. Fuller, P. Chirarattananon, N. Prez-Arancibia, J. D. Greenberg, and R. J. Wood, "A hovering flapping-wing microrobot with altitude control and passive upright stability," in *Proc. EEE/RSJ Int. Conf. Intell. Robots Syst.*, 2012, pp. 3209–3216.

[13] K. Y. Ma, P. Chirarattananon, S. B. Fuller, and R. J. Wood, "Controlled flight of a biologically inspired, insect-scale robot," *Science*, vol. 340, no. 6132, pp. 603–607, 2013.

[14] S. Park, J. Her, J. Kim, and D. Lee, "Design, modeling and control of omni-directional aerial robot," in *Proc. IEEE/RSJ Int. Conf. Intell. Robots Syst.*, Oct. 2016, pp. 1570–1575.

[15] R. Mahony, V. Kumar, and P. Corke, "Multirotor aerial vehicles: Modeling, estimation, and control of quadrotor," *IEEE Robot. Autom. Mag.*, vol. 19, no. 3, pp. 20–32, Sep. 2012.

[16] W. Zhang, M. W. Mueller, and R. D'Andrea, "A controllable flying vehicle with a single moving part," in *Proc. IEEE Int. Conf. Robot. Autom.*, 2016, pp. 3275–3281.

[17] M. W. Mueller and R. D'Andrea, "Stability and control of a quadrocopter despite the complete loss of one, two, or three propellers," in *Proc. IEEE Int. Conf. Robot. Autom.*, 2014, pp. 45–52.

[18] R. Olfati-Saber, "Nonlinear control of underactuated mechanical systems with application to robotics and aerospace vehicles," Ph.D. dissertation, Dept. Elect. Eng. Comput. Sci., Massachusetts Inst. Technol., Cambridge, MA, USA, 2001.

[19] C. K. Gilmore and S. R. Barrett, "Electrohydrodynamic thrust density using positive corona-induced ionic winds for in-atmosphere propulsion," in *Proc. R. Soc. A*, vol. 471, no. 2175, 2015, Art. no. 20140912.

[20] E. Altuğ, J. P. Ostrowski, and C. J. Taylor, "Control of a quadrotor helicopter using dual camera visual feedback," *Int. J. Robot. Res.*, vol. 24, no. 5, pp. 329–341, 2005.

[21] I. Kolmanovsky and N. H. McClamroch, "Developments in nonholonomic control problems," *IEEE Control Syst.*, vol. 15, no. 6, pp. 20–36, Dec. 1995.

[22] *Nine-Axis MEMS MotionTracking Device, MPU-9250*, TDK InvenSense, San Jose, CA, USA, Jan. 2014.

[23] M. Karpelson, G.-Y. Wei, and R. J. Wood, "Milligram-scale high-voltage power electronics for piezoelectric microrobots," in *Proc. IEEE Int. Conf. Robot. Autom.*, 2009, pp. 2217–2224.

[24] M. Karpelson, R. J. Wood, and G.-Y. Wei, "Low power control ic for efficient high-voltage piezoelectric driving in a flying robotic insect," in *Proc. IEEE Symp. VLSI Circuits*, 2011, pp. 178–179.

[25] P.-E. J. Duhamel, N. O. Pérez-Arancibia, G. L. Barrows, and R. J. Wood, "Biologically inspired optical-flow sensing for altitude control of flapping-wing microrobots," *IEEE/ASME Trans. Mechatron.*, vol. 18, no. 2, pp. 556–568, Apr. 2013.

[26] P. Chirarattananon, Y. Chen, E. F. Helbling, K. Y. Ma, R. Cheng, and R. J. Wood, "Dynamics and flight control of a flapping-wing robotic insect in the presence of wind gusts," *Interface focus*, vol. 7, no. 1, 2017, Art. no. 20160080.